

## Indirect pumping of alkali-metal gases in a miniature silicon-wafer cell

J.D. Zipfel<sup>1</sup>,\* P. Bevington, L. Wright<sup>2</sup>, and W. Chalupczak<sup>2</sup>


*National Physical Laboratory, Hampton Road, Teddington, TW11 0LW, United Kingdom*

G. Quick and B. Steele<sup>3</sup>

*INEX Microtechnology Ltd., Herschel Annex, Kings Road, Newcastle upon Tyne, NE1 7RU, United Kingdom*

J. Nicholson and V. Guarrera

*School of Physics and Astronomy, University of Birmingham, Edgbaston, Birmingham, B15 2TT, United Kingdom*

 (Received 26 October 2023; revised 20 May 2024; accepted 25 June 2024; published 23 July 2024)

Atom spin sensors occupy a prominent position in the landscape of quantum technology, as they can combine precise measurements with appealing miniature packages that are crucial for many applications. In this work, we report on the design and realization of miniature silicon-wafer cells, with a double-chamber configuration and integrated heaters. The cells are tested by our systematically studying the dependence of the spin dynamics on the main pump parameters, temperature, and bias magnetic field. The results are benchmarked against centimeter-sized paraffin-coated cells, which allows optimization of the operating conditions of a radio frequency–driven atomic magnetometer. In particular, we observe that, when indirect optical pumping is performed on the two cells, an analogous line-narrowing mechanism appears in otherwise-very-different cell conditions. Competitive results are obtained, with magnetic resonance linewidths of roughly 300 Hz at the maximum signal-to-noise ratio, in a nonzero-magnetic-field setting, and in an atomic shot noise–limited regime.

DOI: [10.1103/PhysRevApplied.22.014056](https://doi.org/10.1103/PhysRevApplied.22.014056)

### I. INTRODUCTION

In recent years, the combination of technological development and the progress made in understanding underlying operating principles has driven atomic magnetometers and comagnetometers from laboratory-based proof-of-principle demonstrations towards a multitude of in-the-field applications. One of the crucial requirements for many real-life implementations, from biomagnetism detection [1,2] to navigation [3], is the miniaturization of the sensor's head. More generally, the reduction of the size, weight, power, and cost envelope of these atomic devices can potentially lower operating costs, and consequently enable mass-scale production. In this context, one of the critical components for the miniaturization of atomic (co)magnetometers is the vapor cell.

The first miniature atomic vapor cells, based on a silicon wafer, were realized as a part of the development of coherent-population-trapping clocks [4–7]. The cell volume is enclosed between glass windows that are attached to a silicon wafer via anodic bonding. Since their first realization, these cells have been built in a variety of configurations, which offer different improvements in performance [8,9]. For example, condensation of the alkali-metal

atoms on the cell windows was averted by the use of gold spots mimicking a temperature gradient [10]. Extension of the cell lifetime, by reduction of the atomic diffusion through the cell walls, has been achieved by coating of the inner surfaces with aluminum oxide [11,12]. Thick wafers, multiple-wafer stacks, or mirrored surfaces inside the cell have been instead used to increase the optical path and thus the number of addressable atoms [13–15]. Finally, in parallel with the development of the cell structure, various methods of alkali-metal deposition have been explored [16]. Because of the novel and specific conditions, many of the engineering solutions introduced in the field of miniature cells also require a complementary understanding of the atomic vapor polarization dynamics in these environments.

In this paper we report on the realization of a versatile, cost-effective, wafer-based atomic cell with a double-chamber arrangement and integrated heating circuit. Separation of the alkali-metal storage from the interaction chamber, as well as engineering of a temperature gradient across the cell, prevents reduction of the optical access and the degradation of the spin coherence due to spurious deposition at the cell windows. Moreover, with the use of azide as an alkali precursor, we can greatly simplify the production process, without any sign of compromising the performances obtained. Our cells are thoroughly tested for

\*Contact author: [jake.zipfel@npl.co.uk](mailto:jake.zipfel@npl.co.uk)

operation in conditions of indirect pumping, a technique that has proven to be resourceful in paraffin-coated cells [17], but that has not been demonstrated elsewhere yet to our knowledge.

Evacuated paraffin-coated cells (without buffer gases) set the metrological benchmark for atomic magnetometers, due to their long coherence lifetimes and the relative simplicity of their pumping dynamics, enabled through theoretical description of measured radio-frequency (rf) spectra. Experimental comparison of the observable dependencies (e.g., linewidth on pump power) can be used to gain direct insight into the pumping dynamics of the more-complex scenario of miniature cells filled with inert buffer gas.

In particular, the focus of the present work is the optimization of the atomic polarization and coherence lifetime in relatively low bias fields, i.e., up to  $10\ \mu\text{T}$ . This regime is of interest for the development of radio-frequency atomic magnetometers for object detection [18] and non-destructive testing [19], as they offer higher sensitivity at low frequencies with respect to alternative techniques.

The measurements are conducted in a pump-probe configuration, where the circularly polarized beam creates a stationary collective atomic spin component, while the linearly polarized probe beam monitors the atomic coherences generated by an rf magnetic field (Fig. 1). The presence of a buffer gas, naturally released by the azide, determines the diffusive character of the thermal atomic motion inside the cell volume [20]. Different contributions to the atomic polarization process are identified through the characterization of the signal's dependence on pump power, and the temperature dependence enables discrimination between different dynamical regimes dominated by optical pumping or spin-exchange collisions (SEC) of optically polarized atoms. The comparison with analogous

measurements taken in a paraffin-coated cell helps in identifying the optimal conditions for operation (i.e., pump parameters and atomic gas temperature), which allow us to obtain competitive performances in the scenario of miniature cells [21,22] with rf resonance widths as good as 300 Hz in nonzero-field operation. In particular, we identify a line-narrowing mechanism in our wafer cells that is due to indirect pumping, and occurs similarly to, but following a dynamic different from, the one observed in paraffin-coated cells.

This paper is structured as follows: First, essential details of the measurement instrumentation are provided. Then, a few aspects of the cell-design, manufacturing, and characterization processes are discussed. A brief summary of the measurement method is followed by the analysis of the rf spectrum's dependence on pump power, recorded at various vapor temperatures and at different magnetic fields.

## II. EXPERIMENTAL SETUP

The measurement setup, schematized in Fig. 1, is enclosed in a Twinleaf cylindrical shield (MS-1LF) to limit the influence of the ambient magnetic field. The static magnetic bias field is produced by a set of coils within the shields. In the current configuration this is limited to about  $4\ \mu\text{T}$  (15 kHz) by the available current sources. In separate measurements, we confirmed that the inhomogeneity of the bias magnetic field over the cell extension is as good as 0.01%, and does not contribute to the signal linewidth. The measurements reported were performed in a temperature range between 290 and 370 K (atomic density  $n_{\text{Cs}} = 3 \times 10^{10} - 1.0 \times 10^{13}\ \text{cm}^{-3}$ ). The cell is enclosed in a 3D-printed holder, and the heater is driven by a current sinusoidally modulated at a frequency of 1 MHz. Pumping is performed by a circularly polarized laser beam, frequency tuned close to the  $6^2S_{1/2}F = 3 \rightarrow 6^2P_{3/2}F' = 2$  transition (cesium D2 line, 852 nm), propagating along the direction of the bias static magnetic field (Fig. 1). The spatial profiles of the pump and probe beams are extended by a beam expander (Thorlabs SM2CP1) and are truncated by a 5-mm diaphragm to produce “top-hat” spatial profiles. The atomic coherence is created by our coupling the polarized atoms to an rf field generated by a small coil located above the cell and aligned along the  $\hat{x}$  axis. The magnitude and phase of the atomic coherence are mapped onto the polarization of the linearly polarized probe beam through the paramagnetic Faraday effect [23,24]. The probe-laser frequency is tuned  $+7.2\ \text{GHz}$  from the  $6^2S_{1/2}F = 3 \rightarrow 6^2P_{3/2}F' = 2$  transition via phase-offset-locking to the pump beam, and propagates orthogonally to the pump beam. The rf resonance signal is measured by a lock-in amplifier referenced to the first harmonic of the rf-field frequency.

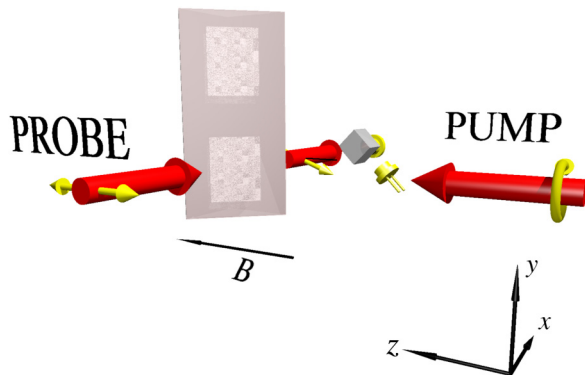


FIG. 1. Measurement setup. The circularly polarized pump beam propagating along the bias-magnetic-field direction,  $\hat{z}$  axis, creates atomic polarization along with SEC. The linearly polarized probe, propagating along the  $\hat{x}$  direction, monitors the atomic coherence precession via the paramagnetic Faraday effect.

### III. SILICON WAFER-BASED CELL

#### A. Layout and manufacturing

During these studies, about 30 vapor cells were used in systematic measurements, with about 100 tested in total. As previously mentioned, the wafer-based vapor cells used in this work have a double-chamber design (Fig. 2). One chamber is used as storage for the alkali precursor, cesium azide, and it is connected to a second chamber, the interaction chamber, where the released Cs vapor interacts with the laser beams. The vapor cell was constructed with an anodic bonded triple stack of BORO FLOAT 33 glass/Si/BF33 glass. The Si layer is 2 mm thick, and the wafer has a diameter of 150 mm. The chambers and channel (0.5 mm thick) were etched with use of a  $\text{Si}_3\text{N}_4$  hard mask and a KOH solution. The chamber etch through the 2 mm-thick cell was done from both sides. A 0.5-mm-thick glass wafer was bonded on one side of the Si to create an open-top chamber. Cesium azide in deionized water solution was dispensed into the storage chamber and then dried. A second 0.5-mm-thick glass wafer was anodically bonded to the Si to create a sealed cell. Before the chambers are sealed, it is possible either to evacuate them to ultrahigh vacuum or to add an additional buffer gas. After bonding, the cesium azide was decomposed by means of broadband UV radiation, resulting in the release of Cs and  $\text{N}_2$ . We tested cells with buffer-gas pressures ranging from 50 to 300 Torr. The cells were extracted from the wafer stack with a dicing saw. The cells have dimensions of  $3 \times 20.2 \times 10.2 \text{ mm}^3$ , with an interaction chamber of  $2 \times 4 \times 4 \text{ mm}^3$ , and weight of 1.24 g.

On-chip heating was fabricated onto the vapor cell to reduce the overall size, decrease power consumption, ease

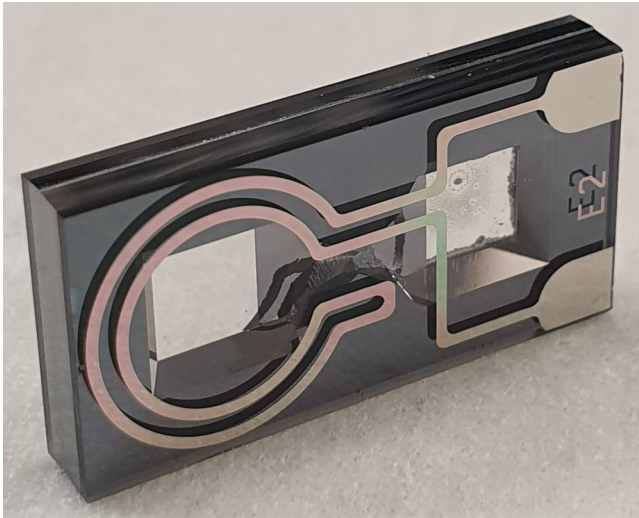


FIG. 2. Silicon wafer-based vapor cell with platinum circuits on both windows, forming the heating unit. On the right side of the cell, the storage chamber containing the cesium sample is visible.

integration, and generate a thermal gradient to inhibit condensation of Cs on the windows of the optical access. COMSOL MULTIPHYSICS simulations, described below, were used to design a Pt heating circuit with minimal stray magnetic field. The design was then transferred to a lithographic mask, which greatly simplified the fabrication process. Standard wafer lift-off resist processing and electron-beam evaporation were used to define the heater tracks and pads. The on-chip heaters were passivated with SU-8 photoresist, hard-baked to make a permanent layer over the Pt tracks.

#### B. Modeling

Modeling and design of the sensor head were done with the finite-element software package COMSOL MULTIPHYSICS, which allowed us to calculate both magnetic field and temperature maps of the cell.

The shape and dimensions of the heating elements were designed to minimize the magnetic flux generated by the resistive heating and to maintain a stable temperature across the interaction chamber without the optical access being blocked. The model also includes the copper pin contacts 1.3 mm wide, 18 mm long, and 0.15 mm thick to more accurately model the temperature. The heater is configured such that the in and out current wires encircle the interaction chamber, and are arranged in close proximity, to minimize the generated magnetic field. Figure 3(a) shows the magnetic flux density  $\mathbf{B}$ , generated by the heating elements with dc input, through the device and through the interaction chamber. It is worth noting that even though  $\mathbf{B}$  is quite large in some parts of the device, and could thus impact the atoms contained in the chambers, the external correction coils and alternating-current input effectively help to minimize this issue. In Fig. 3(b) we show a surface map of the temperature obtained from the model with an input voltage of 13.05 V (the current used in the finite-element models was direct current due to the limitations of the software used). As one would expect, the hottest regions correspond to the heaters themselves, with a maximum temperature of 367 K for this input voltage. The coldest regions in the device are found in the center of the glass windows, as a consequence of the heater design.

#### C. Characterization

We characterized the temperature distribution across the cell by using an Infratec ImageIR 8300 thermal imager with a  $\times 3.0$  M90175 lens, a pixel size of  $5 \mu\text{m}$ , and an integration time of  $466 \mu\text{s}$  to measure the cell's emissivity. The cell was painted with black spray paint to limit the effect of relative emissivity differences between materials (glass, silicon, and platinum). The heaters were wired in series to a direct-current power-supply unit, with a total resistance of  $573 \Omega$  at room temperature. The cell was mounted on a two-axis motorized translation stage to enable systematic



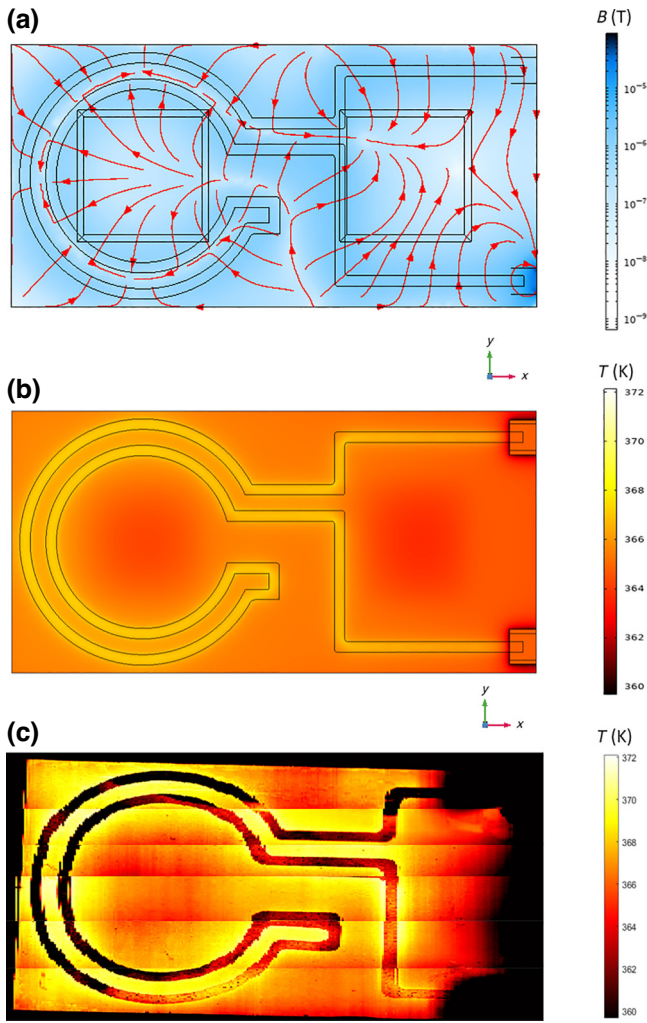


FIG. 3. (a) Modeled magnetic flux density  $\mathbf{B}$  through the device, as generated by the heater with direct-current input. (b) Modeled surface temperature of the cell for an input voltage of 13.05 V. The hottest regions of the model are the platinum heaters, while the coldest regions are the regions above the chambers. (c) Surface cell temperature map measured through thermal imaging. Heater tracks appear darker due to platinum’s lower emissivity.

movement. The cell was then rastered beneath the imager, and the images were subsequently combined. An example of a combined image is given in Fig. 3(c), showing the temperature distribution across the cell, with a temperature in the center of the cell of 365 K.

Figure 4 shows modeled (magenta line) and measured (green line) temperature line traces across the upper surface of the device for three different temperatures. The input voltages used in the model are 13.05, 9.3, and 6.3 V. The interaction and storage chambers are indicated by the blue and red regions, respectively. The Pt wires appear as the three peaks in the modeled datasets, while they appear to be at a lower temperature than the surroundings in the

measured datasets. This is due to the emissivity differences between Si (high) and Pt (low). While this could be avoided with additional sample-preparation steps, we consider it sufficient for the purpose of the present characterization. Both plots agree in the identification of the chamber-window center as a cold spot, the presence of temperature gradients between chambers, and the holder and heater connectors acting as a heat sink. A temperature gradient between two cell chambers ensures that the cesium will condense predominantly in the storage chamber. A higher temperature gradient across the cell between chambers is observed with increasing temperature. This is partially due to the cell mounting and electrical contacts, which act as heat sinks. The temperature drop near the cell support and electrical contacts points to these parts as a major problem in future reduction of the power

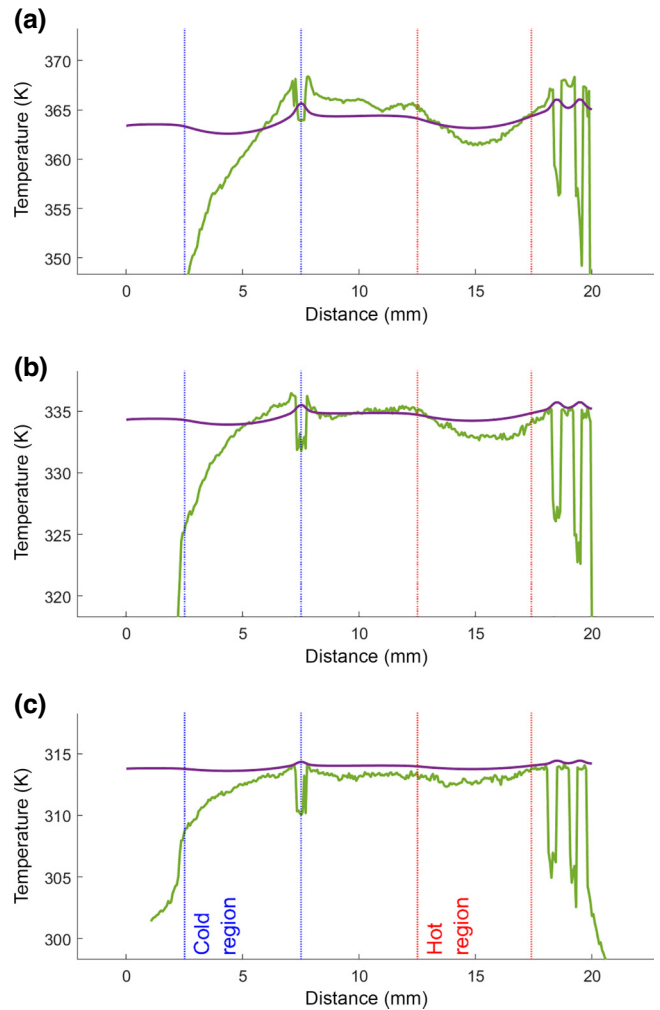


FIG. 4. Modeled (magenta line) and measured (green line) temperature line trace across the upper surface of the device for three temperatures: (a) 365 K, (b) 335 K, and (c) 315 K. The interaction-chamber and storage-chamber regions are marked with vertical dotted lines, red and blue respectively.

consumption of the heating circuit. Agreement in identification of the major properties of the temperature distribution validates the modeling as a useful tool in future work towards further optimization of the cell design.

## IV. DYNAMICS OF THE POLARIZED ATOMIC VAPOR

### A. Indirect pumping

The signal obtained from a magnetometer and, more generally, the dynamics of the atomic polarization and coherence generation are determined by the imbalance between the atomic polarization and coherence creation rate and the various decoherence rates. There are four factors that mainly contribute to these rates: wall collisions, diffusion, optical excitation, and SEC. As it discussed below, optical excitation, with a pumping rate defined by the pump-beam power, and SEC, with a rate defined by the atomic sample temperature, contribute both to the signal (coherence) generation and decoherence. Optical pumping produces stationary collective atomic spin components and consequently contributes to coherence generation. However, in a regime where the pumping rate is greater than the atomic coherence generation rate, it contributes to additional decoherence. In turn, SEC introduce couplings between atoms in the form of exchange of polarization, which could contribute either to dephasing or to transfer of spin temperature, [25] and coherence [26–29].

The term “indirect pumping” refers to a process of generation of an atomic polarization that combines optical excitation and SEC [25]. Indirect pumping has been demonstrated in paraffin-coated cells [17]. In this case, tuning the pump-laser frequency close to the  $6^2S_{1/2}F = 3 \rightarrow 6^2P_{3/2}F' = 2$  cycling transition (for cesium) ensures that polarization within the  $F = 3$  manifold is generated via direct optical pumping, while atoms in the  $F = 4$  manifold are not directly coupled to light. The transfer of polarization from the  $F = 3$  ground-state level to the  $F = 4$  ground-state level, in the low-pump-power regime, is thus realized only via SEC. Indeed, SEC redistribute the angular momentum between the hyperfine ground-state levels, effectively replicating the  $F = 3$  orientation in the  $F = 4$  level. The process is analogous to the so-called spin-exchange optical pumping that involves the transfer of polarization between optically pumped alkali-metal and noble-gas atoms [30]. Eventually, when the pump becomes strong enough to broaden the transition, atoms are also transferred from the  $F = 3$  ground state to the  $F = 4$  ground state [25]. At this point, SEC contribute to the pumping process also by selective relaxation, i.e., relaxation of all Zeeman sublevels but the stretched states from the  $F = 4$  level to the  $F = 3$  level. This combination of off-resonant optical transfer and SEC (referred to as “recycling” in Ref. [25]), produces an additional accumulation of atoms in the stretched state of the  $F = 4$  level.

Conservation of total angular momentum in the SEC process results in immunity of the  $F = 4$  stretched state to SEC decoherence, which becomes visible as a narrowing of the rf resonance linewidth [25]. The linewidth of the rf spectra produced by a low-polarized atomic ensemble at Larmor frequencies below approximately 200 kHz, i.e., in the Larmor frequency range relevant for nondestructive-testing applications, benefits from the narrowing resulting from the degeneracy of all  $F = 4$  coherence frequencies, and consequently from coherence transfer within the  $F = 4$  level [29]. In other words, because of the degeneracy of all  $F = 4$  coherence frequencies, only SEC that cause the  $F = 4$  to  $F = 3$  spin flips contribute to decoherence. Note also that, in paraffin-coated cells, the physical shielding of the atoms from the cell walls allows the atoms to acquire global properties over an integration time set by the fast ballistic dynamics. As a result, all atoms can similarly interact with the pump beam, and between themselves through SEC.

When these conditions are not present, e.g. in cells with buffer gas and no paraffin coating as in the one discussed in the present paper, a different type of indirect pumping, called “diffusive pumping” [20,31,32], can occur. Diffusive pumping consists of optical pumping of the atoms in a small subvolume of the cell, and relying on the diffusive atomic dynamics to transfer polarization to regions of the cell where light is not present. As in the case of the indirect pumping outlined above, this is beneficial to minimize light-induced spurious effects, such as light broadening and frequency shifts. Less evidently, these two techniques share a few more-common features, and might effectively coexist, as we discuss in detail in the following sections.

### B. Measurements

To gain insight into the role of optical excitation and SEC, the dependence of the rf spectroscopy signal on the pump-beam power is studied for various measurement conditions. The rf spectrum (e.g., as shown in Fig. 5) is created by our monitoring the magneto-optical signal as the rf-field frequency is scanned across the magnetic resonance [33]. The rf resonance amplitude provides a measurement of the magnitude of the  $F = 4$  atomic coherence, while its linewidth is related to decoherence processes. The resonance frequency, linewidth, and amplitude of the spectral profile were extracted by our fitting a single Lorentzian, or a combination of two Lorentzian profiles to the rf spectrum (see the discussion below) [20].

In particular, we compare the rf spectroscopy signals obtained in a paraffin-coated cell at room temperature with those obtained in a wafer-based cell at a vapor temperature of 365 K with the same optical excitation on the  $F = 3 \rightarrow F' = 2$  transition. Typical-pump-beam-power scan data recorded in paraffin-coated cells [Fig. 6(a)] show an

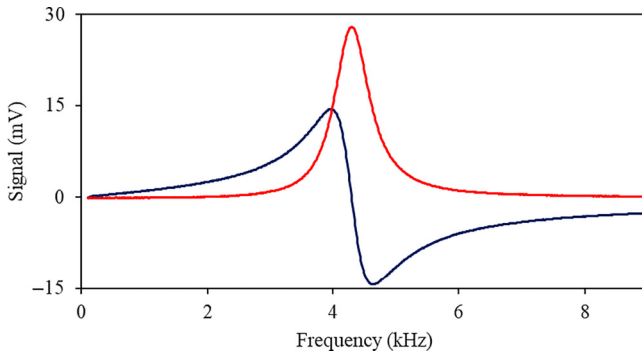


FIG. 5. Radio-frequency spectrum, i.e., dependence of two quadratures of the magneto-optical rotation signal on the frequency of the rf field.

increase of the signal amplitude accompanied by the narrowing of the spectral profile, up to roughly  $200\ \mu\text{W}$ . This narrowing results from the combination of effects described in the previous section. At low powers (less than  $10\ \mu\text{W}$ ), optical pumping on the closed transition generates a population imbalance within the  $F = 3$  level, which is collisionally transferred to the  $F = 4$  level via SEC. For intermediate pump powers ( $10\ \mu\text{W}$  to  $1\ \text{mW}$ ), the addition of optical transfer from  $F = 3$  to  $F = 4$  together with SEC recycling between the two hyperfine ground states effectively favors the occupation of the  $F = 4$  stretched

state. Note that this process is different from the so-called light narrowing, which is caused by the suppression of the spin-exchange broadening at high spin polarization created by a high-power laser [34]. Finally, for pump-beam powers above  $1\ \text{mW}$ , decrease of the signal and broadening of the profile are observed. This is a consequence of the optical transfer rate being much greater than the SEC rate, rather than off-resonant optical coupling to the  $F = 4$  atomic level [35].

We observe that in some parameter subspace the signal amplitude and linewidth measured in the wafer-based cell show a similar dependence on the pump power as in the paraffin-coated cell, despite the different experimental conditions. In more detail, the data recorded in the wafer-based cell show that the linewidth of the rf resonances [in Fig. 6(b)] for pump powers below  $300\ \mu\text{W}$  does not change significantly with the pump-beam power. In the range of pump power between  $300\ \mu\text{W}$  and  $3\ \text{mW}$ , instead, narrowing of the linewidth is observed. In parallel, the dataset in Fig. 6(b) shows also that the amplitude of the  $F = 4$  component increases linearly with the pump power up to roughly  $1\ \text{mW}$ . Then, after reaching its maximum value, the signal amplitude gradually decreases, accompanied by a progressive broadening of the rf spectrum profile. As shown below, this behavior has a common pattern for the pump-power dependencies recorded across the whole temperature range of our measurements (298–366 K).

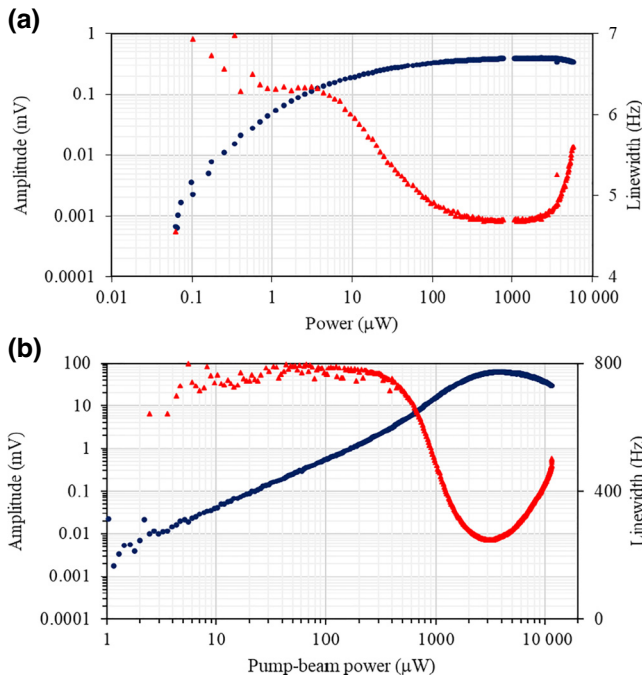


FIG. 6. Amplitude (blue dots) and linewidth (red triangles) of the rf spectral profile as a function of the pump-beam power recorded in room-temperature (a) paraffin-coated cells and (b) wafer-based cells at a temperature of approximately 365 K. The Larmor frequency for both measurements is 15 kHz.

### C. Temperature dependence

To understand the role of SEC in the rf signal generated in the wafer-based buffer cell, we record scans showing the signal pump-power dependencies for atomic vapor temperatures in the range from 298 to 366 K (Fig. 7). Recording the whole pump-power dependence of rf spectra in contrast to a single spectrum at specific conditions allows us to better identify the different mechanisms contributing to the signal behavior.

In particular, no significant change in the linewidths is observed with vapor temperatures below 314 K. This indicates that collisions with the cell walls and the buffer gas dominate over SEC decoherence in the temperature range from 298 to 314 K. In this range, also, the increase of the linewidths observed above  $100\ \mu\text{W}$  reveals the decoherence introduced by the pump beam. This light-induced decoherence rate is common to all the temperature datasets in the high-pump-power regime. The SEC contribution to decoherence increases with increasing vapor temperature, and hence density, at a rate of roughly  $40\ \text{Hz/K}$ . Signal-profile narrowing then appears for temperatures above 353 K, at pump powers above a few hundred microwatts. Notably, the relative narrowing (i.e., the ratio between the narrowing and the linewidth measured at a pump power of around  $100\ \mu\text{W}$ ) scales roughly quadratically with the temperature [exponent equal to 1.7(2)]; see Fig. 8(a).



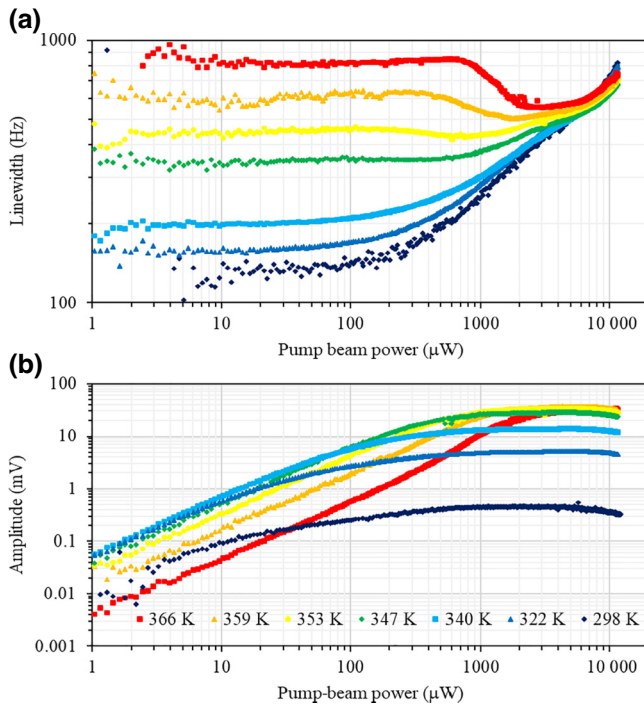


FIG. 7. (a) Linewidth and (b) amplitude of the rf spectral profile as a function of pump-beam power recorded at temperatures ranging between 298 and 366 K. The power dependencies of the rf spectral profile are recorded for the Larmor frequency of 5 kHz. These measurements are performed with 170-Torr nitrogen that is produced by the decomposition of cesium azide.

Moreover, the rate at which the linewidth increases with temperature above 363 K is greater than that for lower temperatures. This can be seen in Fig. 8(b), where the increase in linewidth is shown together with the functional dependence extrapolated from a fit to the data between 314 and 363 K. This suggests that not only is the SEC rate increased with respect to the optical pumping rate (for a given pump power), but also that an additional mechanism is responsible for hampering the pump for higher atomic densities. Additionally, the fact that the linewidth does not significantly vary with temperature for powers greater than 3 mW indicates a high level of global polarization, accompanied by transfer into the stretched state of the  $F = 4$  level.

Spectral-profile narrowing is also accompanied by an increase in the signal amplitude. This is seen as a departure from the linear pump-power dependence evident in Fig. 7(b), and also visible in Fig. 6(b). The same trends as presented in Fig. 7 were observed in a different spherical buffer-gas glass cell with a diameter of 20 mm and with a buffer gas made of 300-Torr neon and 50-Torr nitrogen. From the comparison with this cell, we can also individuate the different contributions to the linewidth in a regime of low pump power and low temperature, due to the different diffusion coefficient (which depends on the buffer-gas pressure) and size of the cells [36]. Finally, for a

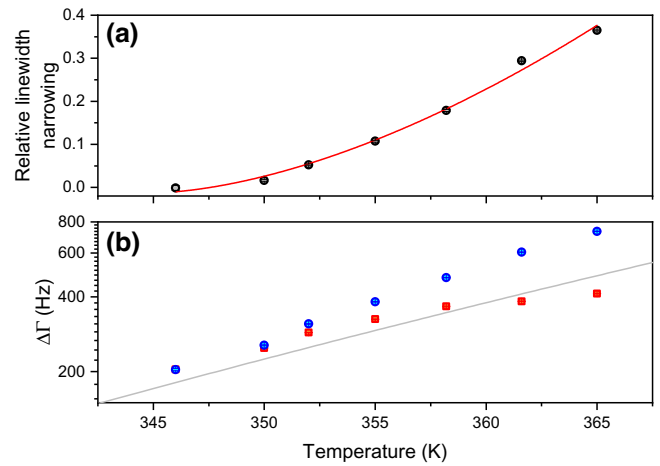


FIG. 8. (a) Relative line narrowing measured as a function of temperature. (b) Increase in linewidth (with respect to room-temperature measurements) as a function of temperature (blue dots) measured between pump powers of 100 and 200  $\mu\text{W}$  and in relation to the maximum line narrowing (red squares). The solid gray line shows the extrapolation from a fit of the temperature dependence below 363 K.

temperature of approximately 363 K, the maximum signal amplitude observed in the pump-power scans starts decreasing below the level obtained at slightly lower temperatures. This is a consequence of the optical density becoming significant enough to prevent the atomic cloud from saturating in the range of laser power available. The trade-off of these parameters is relevant for optimization of the performance of an atomic magnetometer. For instance, optical density greater than 1 guarantees that the sensor can truly operate in a relevant quantum regime, i.e., that the atomic projection noise dominates over the photon shot noise [37]. Noise spectra recorded above 363 K fall in this regime, where atomic projection noise and back-action dominate over photonic shot noise. Preliminary estimations of the sensitivity achievable with the silicon-wafer cell indicate sensitivity at the 23  $\text{fT}/\text{Hz}^{1/2}$  level limited by atomic projection noise and quantum back-action, and at the 10  $\text{fT}/\text{Hz}^{1/2}$  level limited by photonic shot noise (measurements were performed at 372 K and a Larmor frequency of 4 kHz).

#### D. Magnetic field dependence

The SEC-induced decoherence detected in the linewidth of the rf profiles recorded at low pump-beam powers is due to spin flips between  $F = 4$  and  $F = 3$ . This is confirmed by our recording the dependence of the pump-power scans on the bias magnetic field strength in a high-temperature regime (above 363 K). Changes in the linewidth of the rf spectral profiles, recorded at low pump powers, with bias field strength are mainly the signature of the coherence transfer between the  $F = 4$  level and the  $F = 3$  level.

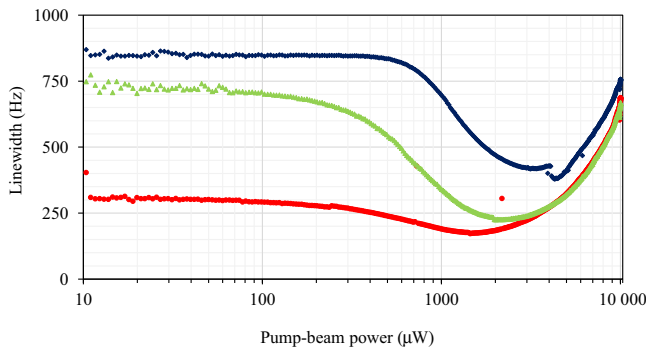


FIG. 9. Linewidth of the rf spectral profile as a function of the pump-beam power recorded at Larmor frequencies of approximately 120 Hz (red dots), approximately 570 Hz (green triangles), and approximately 3.2 kHz (blue diamonds) in a vapor cell of temperature 366 K.

Although the  $F = 3$  and  $F = 4$  atomic coherences oscillate with opposite frequencies, for spectral linewidths exceeding the Larmor frequency, these frequencies become indistinguishable, which allows the macroscopic transfer of the atomic coherences between the levels without phase mismatch. This phenomenon is sometimes referred to as the “spin-exchange-relaxation-free regime” [38–42]. Figure 9 shows the power dependence of the rf-spectral-profile linewidth recorded at Larmor frequencies of approximately 120 Hz, approximately 570 Hz, and approximately 3.2 kHz in a vapor cell of temperature 366 K. These data series show a few generic trends that were observed also in the spherical buffer-gas glass cells. Firstly, the linewidths decrease with decreasing Larmor frequency, with the linewidths recorded at low pump power showing the biggest relative change. Then the linewidth narrowing recorded for pump powers greater than 1 mW becomes shallower. This reflects the decreasing significance of pumping to the stretched state with the decrease of SEC-induced decoherence. Finally, it was noticed that the decrease in linewidth generally results in an increase in the signal amplitude, across a range of the pump powers. The pump power for which the signal maximum is observed decreases with decreasing Larmor frequency. A reduction in the relative light shift was also observed for pump powers below 3 mW. The narrowest linewidth recorded at 366 K is 95 Hz. In similar conditions, we were able to observe linewidths as narrow as 8 Hz in the spherical buffer-gas cell, which is solely due to the difference in diffusion coefficient between the two cells.

### E. Indirect-and-diffusive-pumping model

The generation of spin orientation by optical pumping to the state with maximum (minimum) magnetic quantum number  $m = F$  (or  $m = -F$ ) is an approach to reduce collisional relaxation due to spin-exchange processes between the  $F = 3$  and  $F = 4$  ground-state levels. In wafer cells,

because of collisional broadening due to the presence of a buffer gas (which is on the order of a few gigahertz for our measurements), optical pumping close to the cycling transition  $F = 3 \rightarrow F' = 2$  cannot resolve the hyperfine structure of the excited state  $6^2P_{3/2}$ , thus creating orientation within the  $F = 3$  state (closed pumping) and transferring atoms to the  $F = 4$  state (transfer pumping), already at low pump powers. Overall, this pumping mechanism alone does not work efficiently in promoting the occupation of the  $F = 4$  stretched state. Instead, as outlined in Ref. [25], the combination of optical pumping (with closed and transfer pumping) and spin-exchange collisions (with population replication and recycling between the ground states) greatly increases the stretched-state population and reduces the occupation of the other states, leading to a significant suppression of the collisional relaxation due to SEC. Moreover, it has been shown that without the synergistic action of optical transfer and SEC recycling [25], which happens, for example, when indirect pumping is selective on the closed transition, macroscopic occupation of the  $F = 4$  stretched state becomes less efficient.

In our measurements, we verified that for relatively low pump powers and high densities, the wafer cell’s signal linewidth is still mainly limited by SEC [as in Fig. 6(b)], and only at higher pump powers does narrowing due to the removal of SEC relaxation occur. This suggests that, similarly to the case of closed pumping, the synergistic action of optical transfer and SEC recycling is interrupted at low pump powers, and is re-established at high pump powers. An analysis of our cells shows that despite their small volume, in most of our measurements the atomic sample is optically thick. Even though the beam has a homogeneous radial “top-hat” profile, the decay of the intensity of the pump beam along its direction of propagation effectively limits optical pumping to a subvolume of the cell. In this case, the optically polarized atoms can thermally diffuse out of the pump beam, distributing the atomic polarization in the dark region of the cell, and realizing the condition for the so-called diffusive pumping [20,31,32]. In the range of parameters considered here, the pumping rate (closed and transfer pumping) is typically greater than the rate of SEC, which in turn is roughly comparable to the rate of atomic diffusion. So, in this scenario, the synergistic action of optical transfer and SEC recycling, and consequently the selective relaxation to the  $F = 3$  ground state, is reduced as the optically pumped atoms that occupy mainly the dark subvolume of the cell collisionally interact predominantly with unpolarized atoms, which are not and have not been in direct contact with pump light. If the pump power is increased, the optically pumped subvolume of the cell will increase, and a more-efficient transfer to the  $F = 4$  stretched state will be established. At this point, narrowing of the linewidth, due to suppression of SEC broadening, is observed up to the point where, as in the case of indirect pumping in a paraffin-coated cell, the detected signal



is dominated by light-induced broadening, as visible in Figs. 6(b) and 7.

To model this behavior, we analyze the sublevel populations of the  $F = 4$  ground state that contribute to the detected rf spectrum, an approach similar to the one used in Ref. [25]. In the case of negligible quadratic Zeeman shift, the amplitude of the magneto-optical resonance signal, following a weak rf excitation, is given by [43]

$$S \propto \sum_{m=-F}^{F-1} A_{(m+1,m)} |\hat{\rho}_{m+1,m+1} - \hat{\rho}_{m,m}|^2, \quad (1)$$

with  $A_{(m+1,m)} = |F(F+1) - m(m+1)|^2$ , and the density-operator elements in an ensemble of  $N$  atom  $\hat{\rho}_{m,m} = 1/N \sum_{i=1}^N |m\rangle_i \langle m|_i$ , where  $|m\rangle_i$  are the Zeeman sublevels. In particular, we monitor the population differences in the neighboring sublevels (here shown for a  $\sigma^+$ -polarized pump),

$$r = \min \left\{ \frac{|\hat{\rho}_{F,F} - \hat{\rho}_{F-1,F-1}|^2}{|\hat{\rho}_{m',m'} - \hat{\rho}_{m'-1,m'-1}|^2} \right\}, \quad (2)$$

with  $-F+1 \leq m' < F$ , to get an estimate of the relative amplitude of the signal due to the stretched state. In this picture, a larger  $r$  corresponds to a larger collective occupation of the  $F = 4$  stretched state and to a longer coherence lifetime (provided additional relaxation mechanisms do not intervene).

For an optically thick atomic cloud, the intensity of a resonant light beam decreases as it propagates through the cloud along the  $z$  direction according to the modified Beer's law  $dI(z)/dz = -\tilde{n}\sigma(I)I(z)$ , where  $\tilde{n} = \beta n$  is an effective atomic density, which accounts for the optical transfer of the atoms to the  $F = 4$  ground state, and  $\sigma(I) = \sigma_0/\alpha + I(z)/I_{\text{sat}}$  is the cross section including saturation effects [44]. In this latter expression,  $\sigma_0$  and  $I_{\text{sat}}$  refer to the cycling transition  $F = 3 \rightarrow F' = 2$ , and  $\alpha$  is a parameter that depends on beam polarization, on the structure of the excited state, and on the occupation of different Zeeman sublevels. To simplify the numerical calculations, we consider the pump to be present where  $I(z)/I_0 > 0.1$  (and absent otherwise), where  $I_0$  is the intensity of the beam before it enters the cell. The diffusive dynamics is taken into account by our considering the atoms spatially distributed (on average over our long interrogation time) according to the stable lowest-order diffusive mode in a rectangular cell geometry with depolarizing collisions at the walls  $u_0(z) \propto \cos(k_0 z)$ , with  $k_0$  being the mode's wave number [45]. Then, we attribute a spatially varying occupation of the  $F = 4$  Zeeman sublevels to the local intensity of the pump beam. To do this, we consider an extreme scenario: in the region where the pump is present, optical pumping and SEC are active at the same time; and, where the pump is not present, optical pumping generates stationary polarization without SEC, and then the polarized atoms

undergo SEC only with unpolarized ones (see also [25]). The latter mechanism is meant to reproduce the dynamics of the atoms that are optically pumped but, diffusing out of the pump region, are then allowed to undergo SEC in the dark. In practice, for each value of  $I_0$  we calculate the integrated  $r$  over the lowest-order diffusive mode  $u_0(x)$ , as shown in Fig. 10, and on the basis of on the Zeeman-sublevel occupation we estimate the rate of coherence relaxation due to SEC. The model shows good qualitative agreement with the data. However, line narrowing is observed in the experimental data at lower pump-beam intensities, typically in the range from 0.5 to 30 mW/cm<sup>2</sup>, which is compatible with a theoretical overestimation of the effective atomic density  $\tilde{n}$ . The simple model confirms that effective indirect pumping with suppression of SEC broadening is feasible in these cells, when, at least, roughly half of the volume is optically pumped. Moreover, a rough comparison between the current measurements and the model suggests that the greatest signal-to-noise ratio (SNR) might correspond to a situation where most of the cell volume is (indirectly) optically pumped. Further work, including more-detailed modeling, is needed to clarify the interplay between indirect and diffusive pumping, and its impact on the SNR. As indirect pumping, diffusive pumping is beneficial to minimize light-induced spurious effects. By selectively detecting the signal from the dark subvolume of the cell, or pumping with a transverse nonuniform beam (e.g., a Bessel beam), one could

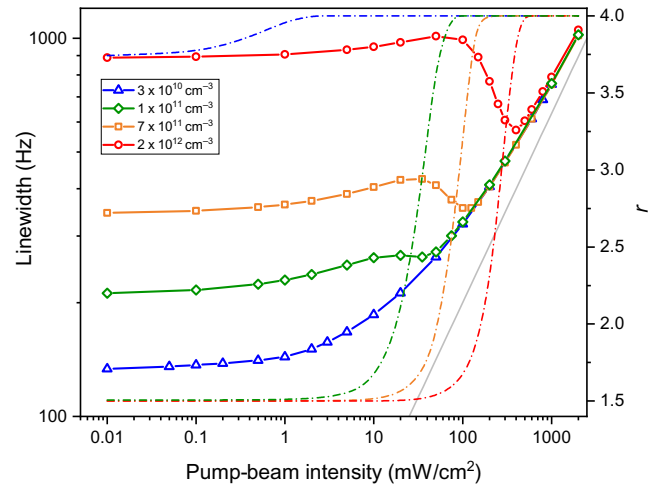


FIG. 10. Estimated values of the relative population of the stretched state  $r$ , as defined in the main text, and linewidth for different pump intensities and atomic densities. The linewidth is the result of a sum of relaxation due to SEC, light broadening (solid gray line), and a bias of roughly 120 Hz derived from the experimental data, and which includes spin destruction at the cell walls. In the calculations we used  $\alpha = 1$ ,  $\beta = 0.3$ , and the cross section of cesium-cesium spin-exchange collisions  $\sigma_{\text{SEC}} = 1.4 \times 10^{-14}$  cm<sup>2</sup>. The amplitude coefficient of the light-induced broadening was kept as a free parameter.

combine more efficiently the benefits of the two pumping schemes, leading to an overall increase of the SNR.

## V. DISCUSSION AND CONCLUSIONS

Despite early claims of the possible benefits of metal condensation at the cell windows [46], in a series of measurements performed with buffer-gas glass cells we have observed that the presence of metal droplets at the cell surface has a negative impact on the relaxation rate of the atomic coherence, and effectively limits the sensitivity of the atomic sensor. Moreover, changing dimensions of the droplets, observed when the cell temperature is varied, results in limited reproducibility of the detected signal linewidth. While we have observed variation in the decoherence rate up to a level of 30% in these glass cells, this level is reduced to only 5% in our wafer cells because of their design, which is meant to minimize the chance of metal-droplet formation within the main chamber. In conclusion, we have presented a robust, simple, and inexpensive realization of a wafer-cell architecture for use in atomic magnetometry, with excellent performances for nonzero-field operation (up to 10  $\mu$ T) and for applications requiring miniaturization. We have individuated the conditions for the indirect-pumping mechanism to reduce both decoherence due to SEC and spurious light effects in these cells, while maximizing the signal amplitude. These conditions correspond to the most part of the cell volume to be optically pumped, which can still be compatible with exploitation of diffusive pumping for further reduction of light broadening. More generally, the multimode diffusive nature of the cells, together with the possibility to control the spatial beam profile of the pump and the probe, opens up new opportunities to further improve the performance of these wafer cells, and to use them for other applications in the realm of quantum imaging and information. Indeed, thanks also to the maturity of the manufacturing process, wafer-based cells are very appealing substrates for the development of atom-photon interfaces [47]. Finally, with the possibility to increase the operation temperature up to a maximum tested value of 543 K, interesting regimes for sensing beyond the standard quantum limit [48] are also within reach of our wafer cells' design.

The data that support the findings of this study are available from the contact author upon reasonable request.

## ACKNOWLEDGMENTS

We acknowledge the support of the UK Government Department for Science, Innovation and Technology through the UK National Quantum Technologies Programme. We thank A. Parsons for critically reading the manuscript, and J. McMillan for help with thermal imaging.

- [1] M. E. Limes, E. L. Foley, T. W. Kornack, S. Caliga, S. McBride, A. Braun, W. Lee, V. G. Lucivero, and M. V. Romalis, Portable magnetometry for detection of biomagnetism in ambient environments, *Phys. Rev. Appl.* **14**, 011002 (2020).
- [2] Yulia Bezsudnova, Lari M. Koponen, Giovanni Baroncini, Ole Jensen, and Anna U. Kowalczyk, Optimising the sensing volume of OPM sensors for MEG source reconstruction, *NeuroImage* **264**, 119747 (2022).
- [3] T. D. Walker and M. S. Larsen, Spin-exchange-pumped NMR gyros, *Adv. At., Mol. Opt. Phys.* **65**, 373 (2016).
- [4] L. A. Liew, S. Knappe, J. Moreland, H. Robinson, L. Hollberg, and J. Kitching, Microfabricated alkali atom vapor cells, *Appl. Phys. Lett.* **84**, 2694 (2004).
- [5] V. Shah, S. Knappe, P. D. D. Schwindt, and J. Kitching, Subpicotesla atomic magnetometry with a microfabricated vapour cell, *Nat. Photonics* **1**, 649 (2007).
- [6] S. Knappe, in *Comprehensive Microsystems*, edited by Y. B. Gianchandani *et al.* (Elsevier, Amsterdam, 2007), Vol. 571.
- [7] J. Kitching, Chip-scale atomic devices, *Appl. Phys. Rev.* **5**, 031302 (2018).
- [8] S. Woetzel, V. Schultze, R. Ijsselsteijn, T. Schulz, S. Anders, R. Stolz, and H. G. Meyer, Microfabricated atomic vapor cell arrays for magnetic field measurements, *Rev. Sci. Instrum.* **82**, 033111 (2011).
- [9] Pawel Knapkiewicz, Alkali vapor MEMS cells technology toward high-vacuum self-pumping MEMS cell for atomic spectroscopy, *Micromachines* **9**, 405 (2018).
- [10] S. Karlen, T. Overstolz, J. Gobet, J. Haesler, F. Droz, and S. Lecomte, in *European Frequency and Time Forum (EFTF)* (Institute of Electrical and Electronics Engineers (IEEE), 2018), p. 91, <https://www.proceedings.com/40065.html>.
- [11] S. Woetzel, F. Talkenberg, T. Scholtes, R. Ijsselsteijn, V. Schultze, and H. G. Meyer, Lifetime improvement of micro-fabricated alkali vapor cells by atomic layer deposited wall coatings, *Surf. Coat. Technol.* **221**, 158 (2013).
- [12] S. Karlen, J. Gobet, T. Overstolz, J. Haesler, and S. Lecomte, Lifetime assessment of RbN<sub>3</sub>-filled MEMS atomic vapor cells with Al<sub>2</sub>O<sub>3</sub> coating, *Opt. Express* **25**, 2187 (2017).
- [13] Y. Pétremand, C. Affolderbach, R. Straessle, M. Pellaton, D. Briand, G. Miletì, and N. F. de Rooij, Microfabricated rubidium vapour cell with a thick glass core for small-scale atomic clock applications, *J. Micromech. Microeng.* **22**, 025013 (2012).
- [14] S. Dyer, P. F. Griffin, A. S. Arnold, F. Mirando, D. P. Burt, E. Riis, and J. P. McGilligan, Micro-machined deep silicon atomic vapor cells, *J. Appl. Phys.* **132**, 134401 (2022).
- [15] T. Dyer, S. J. Ingleby, C. Dunare, K. Dodds, P. Lomax, P. F. Griffin, and E. Riis, Micro-fabricated caesium vapor cell with 5 mm optical path length, *J. Appl. Phys.* **132**, 204401 (2022).
- [16] P. Knapkiewicz, Technological assessment of MEMS alkali vapor cells for atomic references, *Micromachines* **10**, 25 (2019).
- [17] R. Gartman and W. Chalupczak, Amplitude-modulated indirect pumping of spin orientation in low-density caesium vapor, *Phys. Rev. A* **91**, 053419 (2015).

- [18] R. Gartman and W. Chalupczak, Identification of object composition with magnetic inductive tomography, *Rev. Sci. Instrum.* **92**, 115001 (2021).
- [19] P. Bevington, R. Gartman, and W. Chalupczak, Enhanced material defect imaging with a radio-frequency atomic magnetometer, *J. Appl. Phys.* **125**, 094503 (2019).
- [20] P. Bevington, J. Nicholson, J. D. Zipfel, W. Chalupczak, C. Mishra, and V. Guarrera, Optical control and coherent coupling of spin diffusive modes in thermal gases, *Phys. Rev. Res.* **6**, 023134 (2024).
- [21] V. G. Lucivero, A. Zaroni, G. Corrielli, R. Osellame, and M. W. Mitchell, Laser-written vapor cells for chip-scale atomic sensing and spectroscopy, *Opt. Express* **30**, 27149 (2022).
- [22] D. Hunter, C. Perrella, A. McWilliam, J. P. McGilligan, M. Mrozowski, S. J. Ingleby, P. F. Griffin, D. Burt, A. N. Luiten, and E. Riis, Free-induction-decay magnetic field imaging with a microfabricated Cs vapor cell, *Opt. Express* **20**, 33582 (2023).
- [23] Y. Takahashi, K. Honda, N. Tanaka, K. Toyoda, K. Ishikawa, and T. Yabuzaki, Quantum nondemolition measurement of spin via the paramagnetic Faraday rotation, *Phys. Rev. A* **60**, 4974 (1999).
- [24] I. M. Savukov, S. J. Seltzer, M. V. Romalis, and K. L. Sauer, Tunable atomic magnetometer for detection of radio-frequency magnetic fields, *Phys. Rev. Lett.* **95**, 63004 (2005).
- [25] W. Chalupczak, R. M. Godun, P. Anielski, A. Wojciechowski, S. Pustelny, and W. Gawlik, Enhancement of optically pumped spin orientation via spin-exchange collisions at low vapour density, *Phys. Rev. A* **85**, 043402 (2012).
- [26] G. A. Ruff and T. R. Carver, Spin-exchange light modulation by atomic hydrogen, *Phys. Rev. Lett.* **15**, 282 (1965).
- [27] S. Haroche and C. Cohen-Tannoudji, Experimental study of Zeeman light shifts in weak magnetic fields, *Phys. Rev. Lett.* **24**, 974 (1970).
- [28] J. Skalla, G. Wackerle, and M. Mehring, Coherence transfer between atomic transitions of different g-factor by modulated optical excitation, *Opt. Commun.* **127**, 31 (1996).
- [29] W. Chalupczak, P. Josephs-Franks, B. Patton, and S. Pustelny, Spin-exchange narrowing of the atomic ground-state resonances, *Phys. Rev. A* **90**, 042509 (2014).
- [30] T. G. Walker and W. Happer, Spin-exchange optical pumping of noble-gas nuclei, *Rev. Mod. Phys.* **69**, 629 (1997).
- [31] I. A. Sulai, R. Wyllie, M. Kauer, G. S. Smetana, R. T. Wakai, and T. G. Walker, Diffusive suppression of AC-Stark shifts in atomic magnetometers, *Opt. Lett.* **38**, 974 (2013).
- [32] W. Xiao, M. Liu, T. Wu, X. Peng, and H. Guo, Femtotesla atomic magnetometer employing diffusion optical pumping to search for exotic spin-dependent interactions, *Phys. Rev. Lett.* **130**, 143201 (2023).
- [33] W. Chalupczak, R. M. Godun, and S. Pustelny, Radio-frequency spectroscopy as a tool for studying coherent spin dynamics and for application to radio-frequency magnetometry, *Adv. At., Mol. Opt. Phys.* **67**, 297 (2018).
- [34] S. Appelt, A. Ben-Amar Baranga, A. R. Young, and W. Happer, Light narrowing of rubidium magnetic-resonance lines in high-pressure optical-pumping cells, *Phys. Rev. A* **59**, 2078 (1999).
- [35] W. Chalupczak, P. Josephs-Franks, R. M. Godun, and S. Pustelny, Radio-frequency spectroscopy in the dark, *Phys. Rev. A* **88**, 052508 (2013).
- [36] J. Vanier, J. F. Simard, and J. S. Boulanger, Relaxation and frequency shifts in the ground state of  $^{85}\text{Rb}$ , *Phys. Rev. A* **9**, 1031 (1974).
- [37] A. Kuzmich, N. P. Bigelow, and L. Mandel, Atomic quantum non-demolition measurements and squeezing, *EPL* **42**, 481 (1998).
- [38] W. Happer and H. Tang, Spin-exchange shift and narrowing of magnetic resonance lines in optically pumped alkali vapors, *Phys. Rev. Lett.* **31**, 273 (1973).
- [39] W. Happer and A. C. Tam, Effect of rapid spin exchange on the magnetic-resonance spectrum of alkali vapors, *Phys. Rev. A* **16**, 1877 (1977).
- [40] S. Appelt, B.-A. Baranga, C. J. Erikson, M. V. Romalis, A. R. Young, and W. Happer, Theory of spin-exchange optical pumping of  $^3\text{He}$  and  $^{129}\text{Xe}$ , *Phys. Rev. A* **58**, 1412 (1998).
- [41] D. K. Walter and W. Happer, Spin-exchange broadening of atomic clock resonances, *Laser Phys.* **12**, 1182 (2002).
- [42] I. K. Kominis, T. W. Kornack, J. C. Allred, and M. V. Romalis, A subfemtotesla multichannel atomic magnetometer, *Nature* **422**, 596 (2003).
- [43] B. Julsgaard, J. Sherson, J. L. Sorensen, and E. S. Polzik, Characterizing the spin state of an atomic ensemble using the magneto-optical resonance method, *J. Opt. B* **6**, 5 (2004).
- [44] G. Reinaudi, T. Lahaye, Z. Wang, and D. Gury-Odelin, Strong saturation absorption imaging of dense clouds of ultracold atoms, *Opt. Lett.* **32**, 3143 (2007).
- [45] R. Shaham, O. Katz, and O. Firstenberg, Quantum dynamics of collective spin states in a thermal gas, *Phys. Rev. A* **102**, 012822 (2020).
- [46] X. Zeng, Z. Wu, T. Call, E. Miron, D. Schreiber, and W. Happer, Experimental determination of the rate constants for spin exchange between optically pumped K, Rb, and Cs atoms and  $^{129}\text{Xe}$  nuclei in alkali-metal–noble-gas van der Waals molecules, *Phys. Rev. A* **31**, 260 (1985).
- [47] R. Shaham, O. Katz, and O. Firstenberg, Strong coupling of alkali-metal spins to noble-gas spins with an hour-long coherence time, *Nat. Phys.* **18**, 506 (2022).
- [48] J. Kong, R. Jiménez-Martínez, C. Troullinou, V. G. Lucivero, G. Tóth, and M. W. Mitchell, Measurement-induced, spatially-extended entanglement in a hot, strongly-interacting atomic system, *Nat. Commun.* **11**, 2415 (2020).